JGR Earth Surface

RESEARCH ARTICLE
10.1029/2025JF008577

Rapid Seismic and Infrasound Assessment of Large Landslides: A Case Study From Denali National Park and Preserve (Alaska)

Liam Toney[1], Michael E. West[2], Ezgi Karasözen[2], Denny Capps[3], Elaine Collins[1], Kate E. Allstadt[1], Jana Pursley[1], Heather McFarlin[2], Anne Mangeney[4], David Fee[5], Dennis Staley[6], Matthew M. Haney[6], John J. Lyons[6], and John Bellini[1]

[1]U.S. Geological Survey, Geologic Hazards Science Center, Golden, CO, USA, [2]Alaska Earthquake Center, University of Alaska Fairbanks, Fairbanks, AK, USA, [3]Geologic Resources Division, National Park Service, Denver, CO, USA, [4]Institut de Physique du Globe de Paris, Université Paris Cité, Paris, France, [5]Wilson Alaska Technical Center, Geophysical Institute, University of Alaska Fairbanks, Fairbanks, AK, USA, [6]U.S. Geological Survey, Alaska Volcano Observatory, Anchorage, AK, USA

Key Points:

- A large ice–rock avalanche in Denali National Park and Preserve was rapidly detected using operational seismic monitoring
- We use satellite imagery, seismic and infrasound data, oblique aerial photos, and a numerical flow model to characterize the failure
- Key elements of our analysis could be completed in the minutes to hours after failure for future events

Supporting Information:

Supporting Information may be found in the online version of this article.

Correspondence to:

L. Toney,
ltoney@usgs.gov

Citation:

Toney, L., West, M. E., Karasözen, E., Capps, D., Collins, E., Allstadt, K. E., et al. (2026). Rapid seismic and infrasound assessment of large landslides: A case study from Denali National Park and Preserve (Alaska). *Journal of Geophysical Research: Earth Surface*, *131*, e2025JF008577. https://doi.org/10.1029/2025JF008577

Received 12 MAY 2025
Accepted 16 FEB 2026

Abstract Large, rapid landslides are a global hazard that can occur in remote, mountainous areas. Eyewitness reports of landslides and satellite imagery can often be limited or delayed, particularly during inclement weather. However, landslide-generated seismic and infrasound (low-frequency atmospheric sound) waves can be remotely detected in near real-time. This information can significantly expedite characterization and possible landslide response activities. Here, we highlight these capabilities using a 6.1 million m^3 ice–rock avalanche in Denali National Park and Preserve (Alaska). This event was detected via a landslide-specific seismic location and volume estimation algorithm deployed in Alaska, and—notably—by standard earthquake monitoring systems. Following rapid detection of this event, we combined its seismic and infrasound data set with optical, synthetic aperture radar, and oblique aerial imagery, multitemporal digital elevation models, and a numerical flow model to reconstruct its failure timeline and dynamics. We apply array processing to infrasound signals traveling >250 km and find that two precursory events occurred minutes prior to the main failure. We use long-period seismic signals to infer the force exerted by the landslide on the Earth and constrain the rheological parameters of our numerical flow simulation with this result and deposit morphology. The main failure produced a steeply dipping impulsive initial downward force and reached speeds exceeding 60 m/s. This impulsive force generated relatively strong seismic body waves, which contributed to the earthquake system detection. This large, remote Alaska landslide underscores the key value of seismic and infrasound analysis for rapid landslide assessment and motivates efforts to further operationalize these approaches.

Plain Language Summary Large and fast landslides shake the ground, making seismic waves, and disturb the air, creating infrasound waves. Infrasound waves are sound waves so low in pitch that people cannot hear them, yet they can travel very far. This makes seismic and infrasound waves useful for understanding where, when, and how landslides fail. In September 2023, a large landslide of ice and rock occurred in Denali National Park and Preserve, Alaska. We used seismic and infrasound waves generated by the landslide, along with images collected by satellites and by scientists who flew over the landslide the day after it happened, to study the event. We find that the landslide reached speeds greater than 60 m/s (130 mph) and that its volume was about 6 million m^3 (more than twice the size of the Great Pyramid of Giza). We also find that two similar but much smaller landslides occurred a few minutes before the main landslide, and that the material in the main landslide bounced off several ridges on its way downhill. We consider how we can use seismic and infrasound wave data, recorded and sent immediately, to study future landslides from far away.

1. Introduction

Landslides are a worldwide phenomenon, and remote near-real-time detection of these events is important for rapid hazard response. This is especially important when landslides lead to immediately dangerous cascading hazards, such as tsunamis and seiches (e.g., Gauthier et al., 2018; Svennevig et al., 2024), dammed water bodies (Costa & Schuster, 1988), or lahars (e.g., George et al., 2022). Because eyewitness reports of remote landslides are rare, their occurrence often must be deduced from remote data sources such as aerial and satellite imagery and seismic and infrasound (low-frequency sound waves in the atmosphere) data. Satellite imagery lag times and

other limitations leave the near-real-time detection of large (>0.1 million m^3), remote, extremely rapid (>5 m/s; Hungr et al., 2014) landslides primarily in the domain of seismology and infrasound methods.

Seismic and infrasound data have the advantages of high temporal resolution (sampling rates on the order of tens of hertz), absolute timing precision (on the order of milliseconds), and near-real-time data acquisition and telemetry. In addition, existing geophysical networks (e.g., those used for earthquake and/or volcano monitoring) can be used to monitor seismoacoustic signals generated by extremely rapid landslides. However, most operational automated seismic monitoring systems are designed for earthquakes rather than landslides (e.g., Fuchs et al., 2018; Hayes et al., 2019; Lee et al., 2019). Notable exceptions include the near-real-time landquake monitoring system (NRLMS) in Taiwan (Chang et al., 2024; Chao et al., 2017), which determines both location and source mechanism, and the long-period seismic backprojection algorithm of Karasözen and West (2024). Though not operationalized, detection, location, and volume estimation algorithms have also been developed and tested on rockslides in the European Alps (Manconi et al., 2016). Manconi et al. (2022) trade detection speed for enhanced localization capability by including synthetic aperture radar (SAR) amplitude imagery, which is unaffected by cloud cover, into their detection workflow.

Alaska experiences frequent large and extremely rapid landslides due to its extensive steep, glaciated terrain. Many of these landslides occur in remote areas and are not detected until retrospective analysis is undertaken (e.g., Bessette-Kirton & Coe, 2020; Coe et al., 2018), if they are detected at all. Many of these events are classified as rock and/or ice avalanches—extremely rapid flows of fragmented material from rock or icefalls or slides (Hungr et al., 2014). Many large rock/ice avalanches in Alaska have been initially or retroactively detected and characterized using seismic waves. These include the 2016 Lamplugh rock avalanche (Dufresne et al., 2019), the 2015 Taan Fjord rock avalanche (Higman et al., 2018), the 2005 Mount Steller rock–ice avalanche (Moretti et al., 2012), the 2012 Hubbard rock avalanche (Hibert et al., 2017), the 2012 Lituya Mountain rock–ice avalanche (Geertsema, 2012), and ice–rock avalanches on Iliamna Volcano's Red Glacier in 1994, 1997, 2000, 2003 (Huggel et al., 2007), 2008 (Huggel et al., 2008), 2016, and 2019 (Toney et al., 2021). As Alaska geophysical monitoring networks have geographically expanded (Busby & Aderhold, 2020; Freymueller & West, 2024), additional instrumentation has been incorporated. These enhancements have contributed to notable infrasound recordings of recent large events (e.g., 2016 and 2019 Iliamna Volcano avalanches). Hence, Alaska's high rate of large and extremely rapid events coupled with its relatively dense seismoacoustic network result in many well-recorded landslides. However, many remote events still go undetected or lack sufficient auxiliary data (e.g., satellite images, aerial photographs) to properly verify and characterize them (Hibert et al., 2019). Agencies such as the Alaska Earthquake Center (AEC) and the Alaska Volcano Observatory (AVO) often observe these signals on local/regional earthquake and volcano monitoring networks, but they do not systemically log or characterize these events due to personnel and algorithm constraints.

This article uses a large ice–rock avalanche in Denali National Park and Preserve (Alaska) as a case study to highlight rapid seismoacoustic detection and characterization capabilities. First, we provide an overview of this landslide and the associated response actions and basic characterization efforts that were performed in the 24 hr immediately following the event. Then, we outline the data and methods used to further characterize the landslide via combined seismoacoustic and remote sensing imagery analysis and numerical modeling. We present the results of these analyses and interpret them in the context of landslide dynamics. Finally, we discuss the applicability of our methods to future landslides and other geophysical networks, and reflect on the communication and collaboration implications of cross-organization landslide monitoring. Our objectives are to use this large, remote Alaska landslide to (a) demonstrate the rapid assessment capabilities of seismic and infrasound wave analyses, (b) show how these analyses—when combined with Earth observation data and numerical flow simulations—can provide remarkably detailed reconstructions of landslide dynamics, and (c) motivate additional research into operational seismoacoustic landslide monitoring.

2. Overview of the Denali National Park and Preserve Landslide and 24-Hour Response Timeline

On 13 September 2023 at 18:06 local time, a large ice–rock avalanche occurred near Peters Dome, Alaska, in Denali National Park and Preserve (DNPP). This section provides an outline of detection and response activities in the 24-hr window following the avalanche; additional details are available in Text S1 of Supporting Information S1. This event is specifically considered an "ice–rock avalanche" (Hungr et al., 2014), indicating a higher

proportion of ice than rock; hereafter, we refer to it using the generic term "landslide" for simplicity. Unless otherwise noted, all dates and times in this article are in Alaska Daylight Time (AKDT), which is 8 hr behind Coordinated Universal Time (UTC−08:00).

On 13 September 2023 at 18:09, the U.S. Geological Survey (USGS) National Earthquake Information Center (NEIC) automated earthquake system detected a seismic event in DNPP (Figure 1). The seismic event's waveforms were characteristic of a landslide, so NEIC staff contacted the AEC and established the likely source type. Simultaneously, an AEC-hosted landslide-specific seismic detection tool (refer to Section 3.3; Karasözen & West, 2024) detected an event and obtained a preliminary location which was limited by the tool's regional extent at the time (Figure 1 and Figure S1 in Supporting Information S1). Early the following morning (14 September 2023), the AEC notified DNPP staff of the possible landslide and soon after followed up with a volume estimate and a refined location, which placed the event near Peters Dome, a 3,222 m peak about 12 km northwest of the highest peak in North America (Figure 1).

Park staff contacted a local air tour operator; a pilot reported that they had observed a dust cloud at 18:34 on 13 September (Figure 2a), reinforcing the likelihood of a landslide source. Later on 14 September, DNPP mobilized a fixed-wing reconnaissance flight which confirmed the landslide and provided the first photographs of the site (e.g., Figures 2b–2d). On the afternoon of 14 September, University of Alaska Fairbanks (UAF) researchers used seismic data to independently infer that the landslide had traveled to the north-northwest over a duration of about 80 s. By examining infrasound data, they also concluded that two smaller pre-event landslides occurred several minutes before the main failure.

The rapid aerial reconnaissance mission provided direct observational verification. However, for the Peters Dome landslide, preliminary estimates of the following basic event characteristics were made *remotely* within 24 hr, using seismic and infrasound data alone:

- Location
- Volume
- Duration
- Trajectory
- Timing of failure sequence

Figure 3 shows a visual representation of this timeline. The following section describes the data and methods used to determine the above characteristics, as well as subsequent analyses that allowed us to refine our understanding of the event sequence and its dynamics—to a rare level of detail—using data sets and methods not typically available or readily applicable in the 24-hr response window.

3. Data and Methods

3.1. Earthquake System Detection and Location

The NEIC and AEC both operate near-real-time earthquake detection systems. This event was sufficiently large to be automatically detected less than 3 min after the origin time by NEIC monitoring systems and was confirmed by AEC seismologists as a potential landslide and added to the AEC catalog. AEC procedures for processing landslide events include only using *P* seismic phase arrivals, setting large arrival time errors, and fixing the event depth at 0 km. The event was updated in the AEC catalog 2 days later by AEC seismologists with the verified location provided by the DNPP reconnaissance flight, and pushed to the Advanced National Seismic System (ANSS) Comprehensive Earthquake Catalog.

The NEIC runs a deep-learning-based seismic phase classifier as part of its operational workflow. This classifier assigns a phase label (*P*, *S*, or noise) and an associated confidence to each pick (Yeck et al., 2021). This information is stored along with the pick time and station information and is available for retroactive analysis, which was performed for this event.

3.2. Infrasound Array Processing

The Peters Dome landslide produced infrasound signals recorded coherently on four permanent infrasound arrays across Alaska, located between 250 and 300 km from the landslide (locations in Figure 1). An infrasound array is a collection of individual infrasound sensors arranged such that travel time differences between wave arrivals at

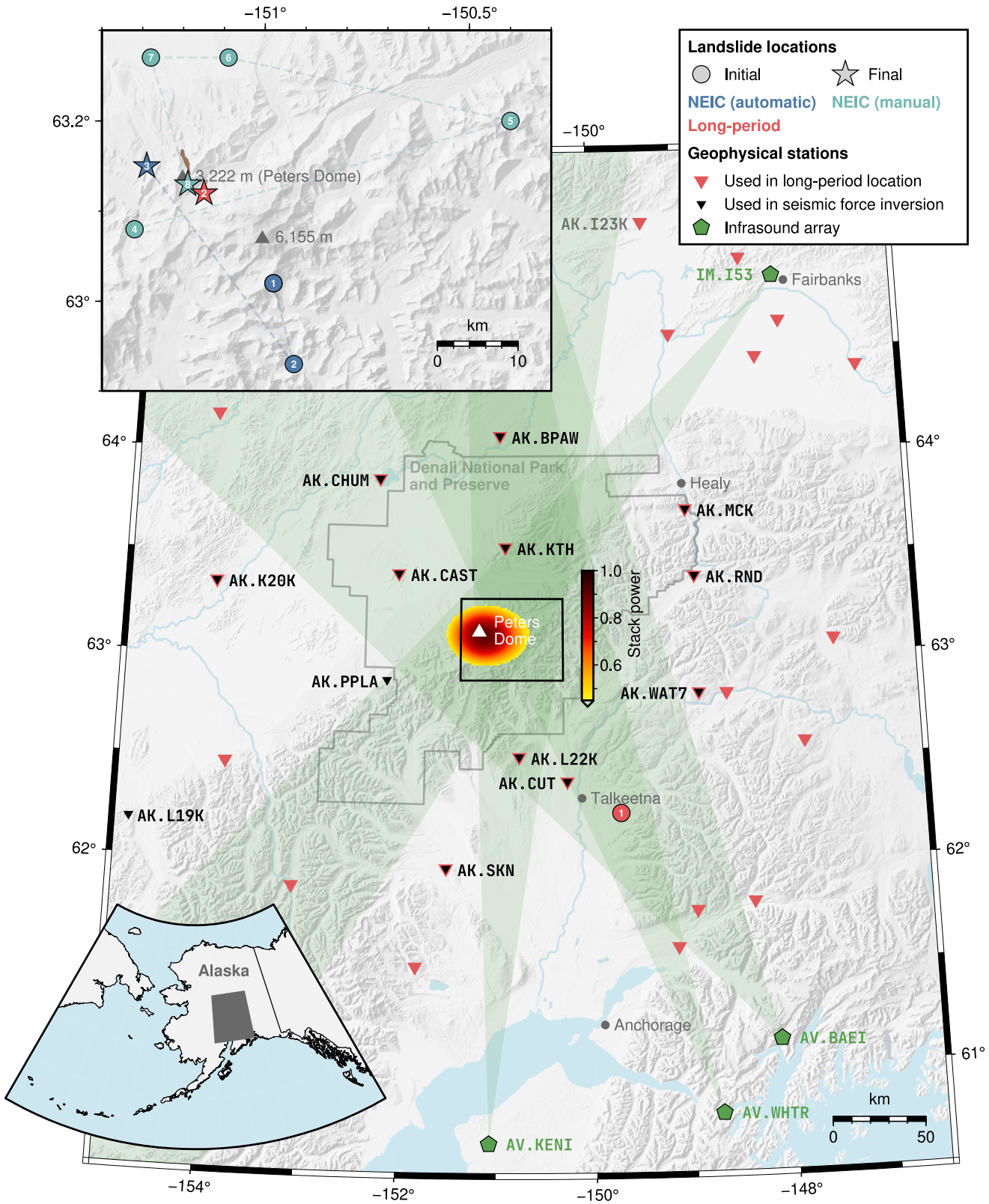

Figure 1.

sensor pairs can be used to determine the back azimuth (the direction sound arrived from) and apparent velocity of waves traveling across the array (Bishop et al., 2020). Infrasound array processing simultaneously produces a measure of the coherence of the arrival, which allows for the separation of incoherent noise sources such as wind. Multiple arrays can be used to form cross-beam locations (Marchetti & Johnson, 2023; Matoza et al., 2017). Infrasound from the landslide was also visible on a few individual infrasound sensors, but here we focus on array data due to the advantages detailed above.

We process infrasound data from the four arrays using 15 s windows with 90% overlap (except for array IM.I53, where we use 30 s windows with 80% overlap to accommodate this array's larger aperture). Infrasound data are bandpass filtered with the lower passband between 0.1 and 0.8 Hz and the upper passband between 4 and 8 Hz, depending on the local noise environment at the array. We threshold the resulting detections using a median cross-correlation maximum of 0.7. We compute the mean and standard deviation of window back azimuth values above this threshold and use these to define a back azimuth swath of the mean back azimuth +/− two standard deviations. We compute potential infrasound source back azimuths for each array and determine the common intersection of all back azimuths to define a source polygon, as illustrated in Figure 1. We do not correct back azimuths for sound advection from horizontal cross-winds (De Negri & Matoza, 2023).

3.3. Long-Period Seismic Detection, Location, and Volume Estimation

The AEC hosts a near-real-time landslide detection algorithm designed to monitor landslides (Karasözen & West, 2024). Every 30 s, the grid search algorithm backprojects 3 min of continuous seismic data from stations within a two-degree radius. Time-shifted waveforms are measured for similarity (i.e., waveform coherence) in the 20–100 s period band using an amplitude stacking algorithm with a wavespeed of 3.4 km/s. If the waveform coherence exceeds a configured threshold, the algorithm estimates the location and approximate volume of a potential landslide. There is a four-minute time delay between detection and notification due to the time needed to gather sufficient data to locate the event, along with the time required for seismic wave propagation. Refer to Karasözen and West (2024) for implementation details.

For the Peters Dome landslide, the initial location was far from the ultimate location because—in September 2023—the operational grid (5 km resolution) was built for landslide monitoring in the Prince William Sound coastal region of Alaska and thus did not extend to encompass the DNPP region. Despite the misaligned waveforms resulting from a detection at the grid edge rather than the true location, the detection was clear (Figure S1 in Supporting Information S1). Upon identifying this landslide, the AEC re-applied the algorithm to a 4°E–W by 2° N–S grid centered on DNPP using a finer grid with 1 km resolution.

3.4. Long-Period Seismic Force Inversion

The substantial long-period (>10 s) seismic energy generated by the Peters Dome landslide motivated us to perform a force inversion analysis to recover the failure dynamics of the event. Seismic force inversions use long-period displacement waveforms recorded on seismometers surrounding the event to infer a spatially static, time-varying 3D vector $\mathbf{f}(t) = (f_Z, f_N, f_E)$ of the forces exerted on the Earth by bulk landslide motion (e.g., Allstadt, 2013; Ekström & Stark, 2013; Moretti et al., 2012). The so-called "force-time function" $\mathbf{f}(t)$ can then be used to derive velocity and trajectory information and interpret event dynamics. Under simplifying assumptions, the components of $\mathbf{f}(t)$ are equal in magnitude, but opposite in sign, to the mass of the landslide multiplied by the acceleration of its center of mass. We use the Python code *lsforce* (Allstadt & Toney, 2020; Toney & Allstadt, 2021) to perform the inversion.

Figure 1. Map of automated and manual Peters Dome landslide locations and geophysical stations used in analyses. Individual geophysical stations are shown as inverted triangles. Red fill indicates stations with seismometers used in the long-period (20–100 s) location, while black fill indicates those used in the force inversion (markers overlap for stations used in both procedures). Infrasound arrays are indicated by green pentagons; array back azimuth swaths are shown as green translucent patches. Initial and final long-period seismic landslide locations are shown as a red circle and red star, respectively. The stack function for the final long-period location is plotted with a yellow-red-black color scale. Landslide locations from the National Earthquake Information Center (NEIC) are shown in the top-left inset as blue circles and a blue star (initial and final automated locations) and cyan circles and a cyan star (initial and final manual locations). The region outlined in gray in the main map is the boundary of Denali National Park and Preserve, and relevant mountain peaks are shown as labeled upright triangles. The total footprint of the landslide is shown in the top-left inset as a brown patch. Basemap vector data are from the Global Self-consistent Hierarchical High-resolution Geography database (Wessel & Smith, 1996).

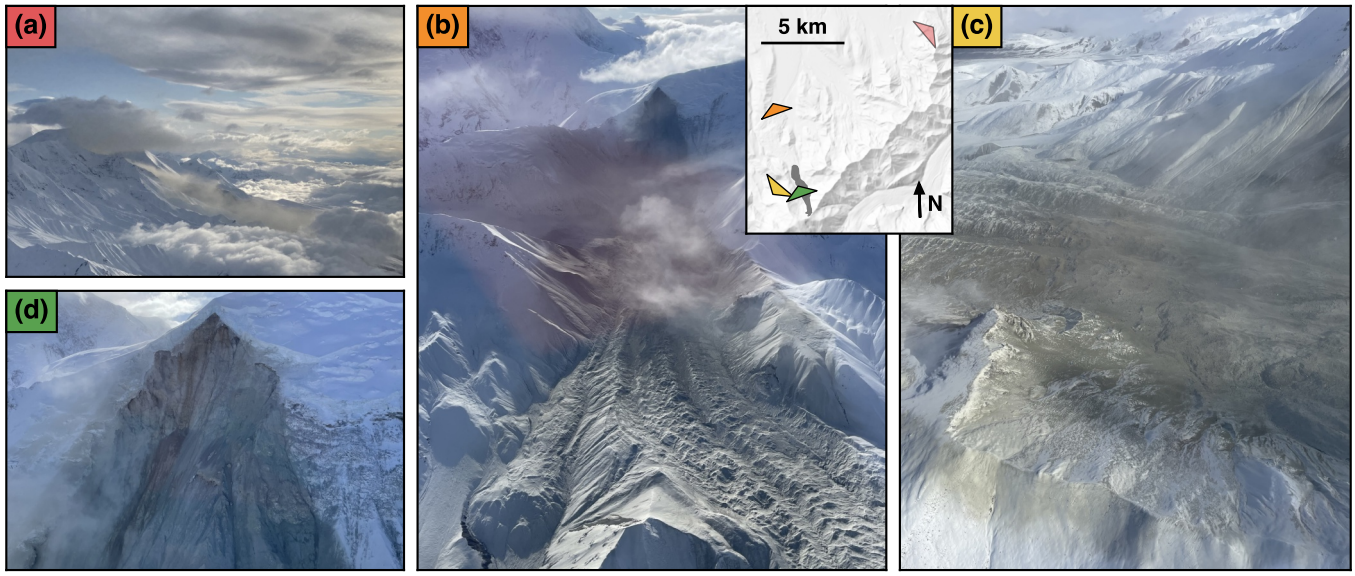

Figure 2. Oblique aerial photos of the Peters Dome landslide. (a) Photograph acquired on 13 September, approximately 30 min after the landslide, by a local air tour operator showing a dust cloud from the landslide in the center of the image. The look direction is approximately southwest. Photo credit Aine Roberts/Denali Air. (b) View of the entire source and deposit area. The look direction is approximately south-southeast. The furrowed surface in the foreground is an unnamed glacier flowing north from Peters Dome. (c) View of the deposit and dust-covered areas in its vicinity. Look direction is approximately northeast. (d) Source area of the landslide. The look direction is approximately south-southeast. Map inset shows locations and look directions of photos; note that the location of photo (a) is only approximate and that photos (a–d) spiral counter-clockwise toward the landslide source area. Photos (b–d) were acquired on a National Park Service fixed-wing reconnaissance flight on 14 September (the day following the landslide); photo credit Denny Capps/National Park Service.

Our force inversion uses data from 13 stations located 48–216 km from the landslide (selected stations are similar to those used for the long-period detection, refer to Section 3.3 and Figure 1). We set the point force location, which remains static per the assumptions of the method, at the center of mass of the landslide source area. We bandpass filter waveforms between 15 and 200 s. The short-period corner is chosen such that microseismic noise is excluded; the long-period corner is selected to fully encompass the duration of the event and minimize the effect of band-limited input data on the inverted force magnitudes. Data are inversely weighted by their noise levels in a

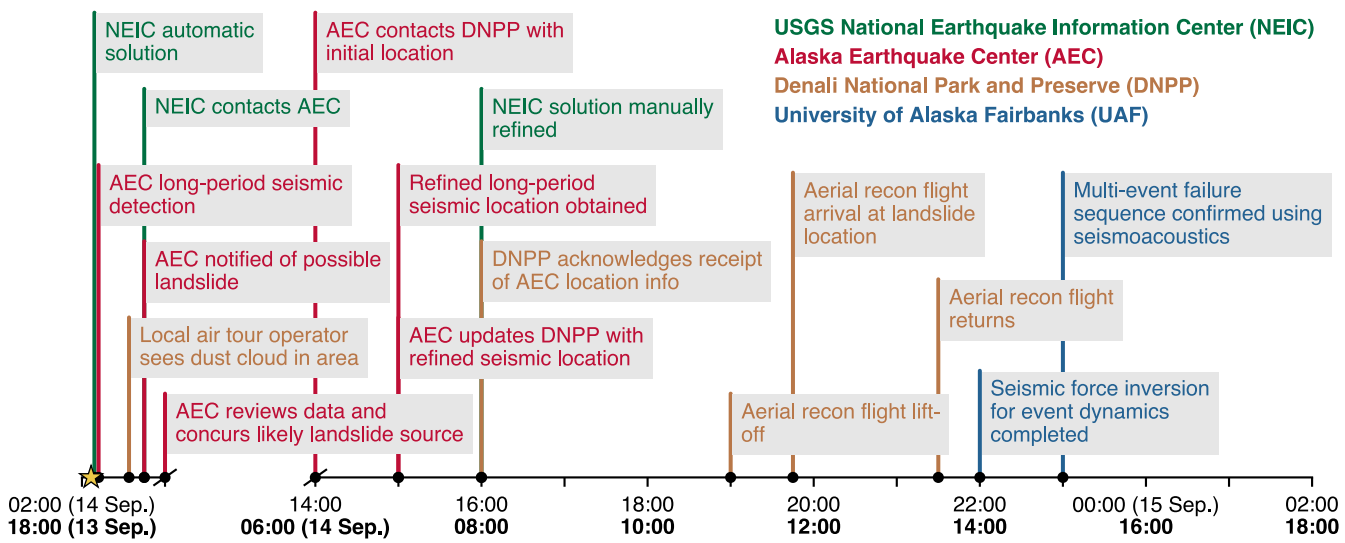

Figure 3. 24-hr response timeline for the Peters Dome landslide. Times are shown in both UTC (top) and AKDT (bottom, in boldface). The break in the *x*-axis corresponds to night in local time. Text colors indicate which organization was involved in the specific response task or event. The yellow star indicates the time of the main landslide failure. USGS, U.S. Geological Survey.

90 s window prior to the data start time. We perform jackknifing to assess model uncertainty by running 100 iterations of the inversion, each time randomly discarding half of the waveforms. We roughly estimate the trajectory of the landslide center of mass from $\mathbf{f}(t)$ by twice-integrating the forces and dividing by a mass autocomputed from a target runout distance, as in Toney et al. (2021).

3.5. SAR Amplitude Image Differencing

In the limited optical and oblique aerial imagery available post-event, we noted considerable dust present along the debris track and deposit areas (Figures 2c and 4a) of the Peters Dome landslide. This complicated delineation of the total area of the landslide, as the boundary between substantial debris deposit and a mere thin dust layer was not evident in optical imagery. We turned to SAR imagery to alleviate this issue. SAR amplitude imagery records the amount of backscattered energy from a surface. For debris traveling onto a relatively smooth substrate, the emplacement of material results in an increase in amplitude in the post-event image due to increased scattering from the rougher debris-covered surface (Mondini et al., 2021). We define a SAR amplitude difference image using Sentinel-1A images from 9 and 21 September 2023 (refer to Figure 4b). The 10 m resolution images are speckle-filtered and radiometric terrain correction is applied. We compute the mean of the VV (vertical transmit, vertical receive) and VH (vertical transmit, horizontal receive) radar wave polarizations for each image date as a noise reduction technique and compute the log difference between pre- and post-event mean amplitude images. We manually delineate the deposit area of the landslide from this SAR amplitude difference image; the source area definition method is explained in the following section. We do not use the SAR amplitude difference image to define the steep source area because of limitations inherent to the side-looking geometry of SAR satellites when imaging steep terrain (Mondini et al., 2021).

3.6. Post-Event Digital Elevation Model Creation and Differencing

As a basic quantitative measure of landslide size, as well as to inform our numerical flow modeling (described subsequently in Section 3.7), we estimated the landslide source volume using digital elevation model (DEM) differencing. The pre-event DEM is from ArcticDEM (Porter et al., 2023)—it is created from stereo optical imagery pairs acquired on 3 November 2020, the closest pre-event date for which imagery is available. We created the post-event DEM using WorldView stereo images acquired on 27 October 2023, the closest post-event stereo pair available, collected approximately 1.5 months after the landslide. We used the Surface Extraction from TIN-based Searchspace Minimization (SETSM) software (Noh & Howat, 2017) to create a 2 m resolution DEM.

We aligned the post-event DEM to the pre-event DEM using CloudCompare, a 3D point cloud processing software (https://github.com/CloudCompare/CloudCompare). Stable regions (e.g., ridges) surrounding the landslide region were extracted from the pre- and post-event DEMs. Neither DEM was available to us as a point cloud, so we converted both to point clouds within CloudCompare and aligned the post-event data to the pre-event data in these stable regions using the software's iterative closest point automatic alignment feature. The resulting transformation matrix was then applied to the full post-event point cloud, after which the point cloud was exported and rasterized using the LAStools software (https://lastools.github.io/).

We subtracted the post-event DEM from the pre-event DEM to obtain an elevation difference raster (Figure 4c). The source region, which is required for estimating the initial volume, is delineated by tracing the −10 m contour in the difference raster. We use this contour to accommodate vertical error in the DEM difference calculation (refer to the following paragraph). The post-event DEM has holes in the source region due to steep topography and shaded areas in the source optical images. We patch the holes in the source region of the post-event DEM by defining profiles orthogonal to the dip direction of the source region. We define both a set of best-fit (fit to valid data in the delineated source region) parabolic profiles, and a set of linearly interpolated profiles. We obtain a source volume from the patched evacuated source area for both the parabolic fit and the linear fit. The purpose of the linear fit is to establish an end-member lowest volume estimate to constrain uncertainty associated with patching the hole in the source region.

We use the methods of Allstadt et al. (2024) to estimate the uncertainty of these volume estimates using standard error propagation with covariance. This approach uses the standard deviation and spatial correlation distance estimated from multiscale model-to-model cloud comparison (M3C2) vertical change estimates between the pre- and post-event DEMs in stable areas and assumes that those statistics are representative of the statistics of the uncertainty over the (patched) source area. The spatial correlation distance of the M3C2 elevation change in stable

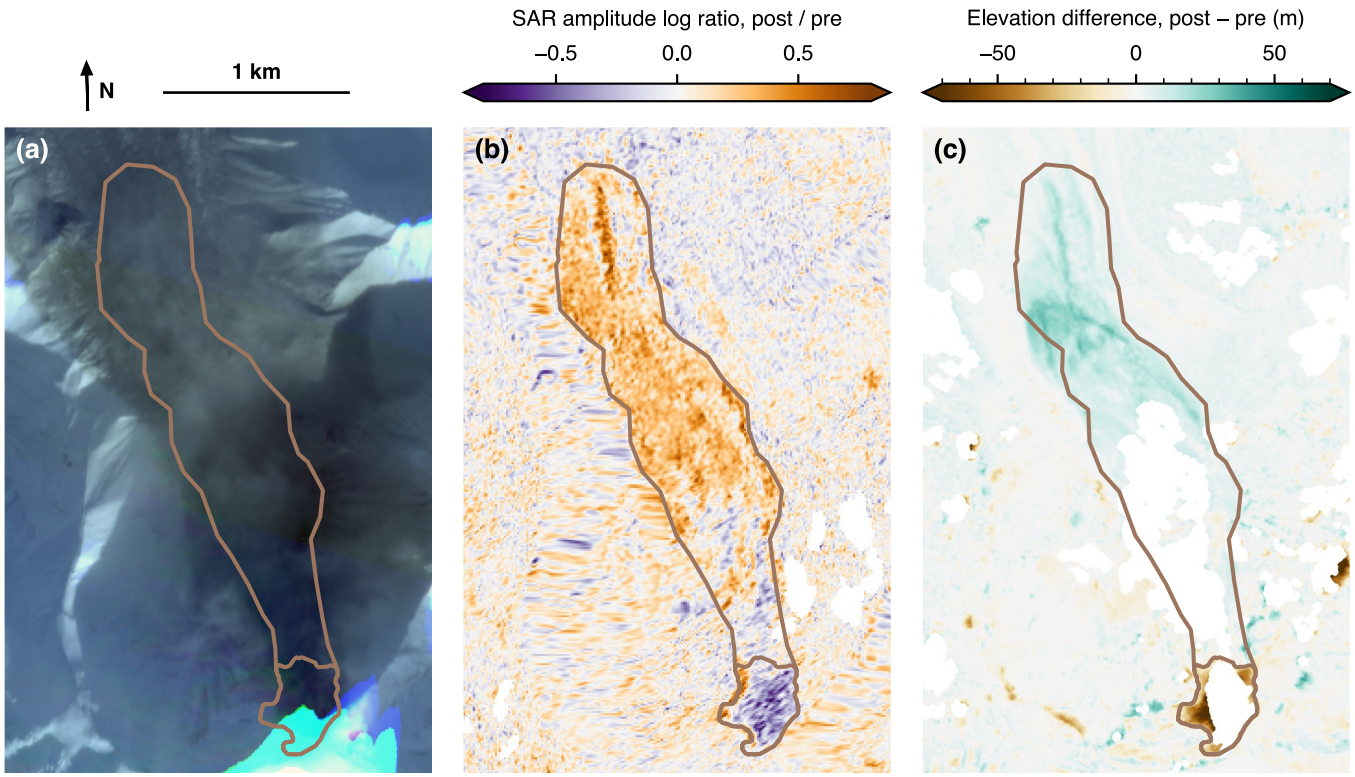

Figure 4. Geospatial characterization of the Peters Dome landslide. (a) Optical satellite image acquired on 14 September. Imagery © 2023 Planet Labs PBC. (b) Log ratio between synthetic aperture radar (SAR) amplitudes of Sentinel-1 images acquired on 9 and 21 September. Positive (orange) values indicate that the surface became brighter (i.e., rougher) in the post-event SAR amplitude image. Images processed by ASF DAAC HyP3 2024. Contains modified Copernicus Sentinel data 2023, processed by ESA. (c) Difference between digital elevation models (DEMs) from 3 November 2020 and 27 October 2023. The broad lobe-shaped positive elevation difference ~1 km from the deposit toe is related to glacial surging between pre- and post-DEM dates and is not part of the landslide deposit. In all panels, the brown outlines indicate the source region and total area of the landslide.

areas is estimated by fitting a spherical model to an empirical semivariogram generated from a random sampling of elevation change differences between 120,000 pairs of points. The M3C2 standard deviation in stable areas is 5.3 m and the spatial correlation distance (range) is estimated to be 96 m. This indicates that the background change in stable areas is minimal between pre- and post-event DEMs.

We additionally compute a volume estimate using an empirical source area–volume scaling relationship with bedrock scar geometry parameters from Larsen et al. (2010). We use the bedrock scar parameters because photos of the source area (Figure 2d) clearly indicate that the failure was structurally controlled. However, because there was significant snow and ice in the source area, we use this relationship mainly as another constraint on the DEM differencing results. The relation for volume V from source area A is

$$V = \alpha A^{\gamma}, \tag{1}$$

where $\log(\alpha) = -0.63 \pm 0.06$ and $\gamma = 1.41 \pm 0.02$. The units of α are $m^{(3-2\gamma)}$, γ is unitless, and A has units of m^2.

3.7. Numerical Flow Modeling

Given the robust constraint on landslide deposit extent, volume, and dynamics provided by our geospatial and seismic analyses, we conducted numerical flow modeling for the Peters Dome landslide. The motivation was to use the model to assist in interpreting the event dynamics suggested by the seismic force inversion. We use the SHALTOP numerical flow modeling software (Lucas et al., 2014; Mangeney et al., 2007). SHALTOP uses a depth-averaged thin layer approximation to model flow over arbitrary two-dimensional topography accounting for centrifugal forces related to complex curvature effects (Peruzzetto et al., 2021). The model requires a basal topographic surface and a source geometry (3D volume) of mobilizable material. We excavate a smoothed

version of the parabolic fit source thickness distribution from DEM differencing (refer to Section 3.6) from the pre-event DEM to obtain the basal topography. The mobile material is the smoothed source thickness distribution; the volume of this material is stated in Section 4.1. Our 3 km E–W by 5 km N–S domain has a grid spacing of 20 m, the simulation time step is 1 s, and the simulation duration is 80 s.

SHALTOP implements many rheological models, each having one or more parameters. We use the simple Coulomb rheology, wherein the friction coefficient μ is derived from a single parameter—the friction angle, δ:

$$\mu = \tan(\delta). \tag{2}$$

Moretti et al. (2020) demonstrated that forces inferred via seismic inversion are one of the best constraints for recovering landslide parameters such as volume and dimensions of the released mass, as well as basal friction. Hence, we select the friction angle for SHALTOP by iteratively running models with various parameter values and comparing the model results with (a) the measured deposit extent and (b) the seismic force inversion results. This approach is conceptually similar to that used in Mitchell et al. (2022). Specifically, we compute the total wetted area from the SHALTOP simulation and calculate the trimline ratio between this and the measured source and deposit footprint (refer to Section 3.5), as proposed in Galas et al. (2007). We also compute the center-of-mass force time series from the SHALTOP simulation and compare, via cross-correlation, with $\mathbf{f}(t)$ from the seismic inversion. We combine these deposit trimline ratio and force cross-correlation measurements into a single normalized misfit metric (with equal weights for both contributing measurements) and use a grid search to find the optimal friction angle δ. We search over the range 15–19° in increments of 0.2°. A density is required to compute the SHALTOP center-of-mass force time series. We select a density, rounded to the nearest 100 kg/m^3, which best matches the maximum downward force observed in the seismic inversion force time series.

4. Results and Discussion

4.1. Location, Deposit Shape, and Volume

Our combined rapid characterization and subsequent analysis efforts provide detailed information about the Peters Dome landslide. The coordinates of the center of mass of the source area of the landslide are 63.1423°, −151.1871°. This location falls within the back azimuth swaths of all but one infrasound array, AV.WHTR (refer to Figure 1). It is within 4 km of the final long-period seismic detection (red star "2" in Figure 1 inset) and 6 km of the NEIC final automated solution (blue star "3" in Figure 1). The relative location error of the long-period seismic detection is 15 km, and the coherence is high, at approximately 0.9. Our estimate of the origin time from the nearest seismometer AK.KTH is 14 September 2023 02:06:35 UTC, with an uncertainty of 15 s. The origin times from the NEIC and AEC earthquake monitoring systems (https://earthquake.usgs.gov/earthquakes/eventpage/ak023bt2cfip) both fall within this uncertainty range.

The landslide source and deposit areas are outlined in Figure 4. The vertical drop of the landslide H is 1,300 m, and the along-path horizontal length L is 3,400 m, resulting in an H/L ratio of 0.38 (measurements are crown-to-toe; refer to Corominas (1996)). We are unable to estimate the final center-of-mass location from DEM differencing due to changes in the glacier over which the landslide flowed, but from the numerical model, the center-of-mass vertical drop H_{COM} is 920 m, and L_{COM} is 2,200 m, resulting in an $(H/L)_{COM}$ ratio of 0.42 and an effective friction angle of 23°. The total area of the landslide footprint (source and deposit) is 1.5 million m^2.

Using DEM differencing, we estimate the landslide source volume to be 6.1 million m^3 (Table 1). This estimate is for the parabolic fit in the source region; the linear fit naturally yields a lower source volume (5.1 million m^3). We use the parabolic fit as the source volume for SHALTOP modeling (refer to Section 3.7) because it produces a better fit to the inverted seismic forces. The standard deviation for these estimates (refer to Section 3.6) is 0.2 million m^3. These measurements compare favorably with an independent preliminary volume estimate from the seismic wave amplitude empirical scaling relationship of Karasözen and West (2024) (4 million m^3; refer to Text S1 in Supporting Information S1). Using the source area-volume scaling relationship (Equation 1) with a source area of 140,000 m^2 derived from DEM differencing (refer to Section 3.6), we obtain a volume estimate of 4.2 million m^3 with low and high estimates of 3.2 and 5.6 million m^3. These bounds are determined by propagating uncertainties in the scaling parameters. It is difficult to define the source area geometry due to oversaturation and dust near the headscarp present in the 14 September optical image, so the source area scaling estimate of volume is uncertain. Furthermore, the bedrock scaling parameters from Larsen et al. (2010) do not account for ice and snow

Table 1
Source Volume Estimation Methods Used in This Study

Method	Data required	Volume (10^6 m^3)	How used
Long-period seismic amplitude volume regression (Karasözen & West, 2024)	Seismic waveforms	4	Initial, rapid indication of size
Source area–volume scaling (Larsen et al., 2010)	Satellite imagery from which source area polygon can be mapped	4.2 (3.2–5.6)	Comparison to DEM differencing
DEM differencing	Pre- and post-event DEMs	6.1 (4.9–6.3)	Best estimate of volume, used in numerical model

Note. Volume uncertainties are provided as ranges in parentheses where available.

in the source area. We note that additional failures occurring between pre- and post-event acquisition times of our DEM input data could result in an overestimation of the source volume (i.e., because the estimate includes additional failures besides the main failure). However, seismic signal energies for noted sub-events (Figure S2 in Supporting Information S1) indicate that these extra volume contributions are small enough relative to the main failure volume to be negligible compared to other sources of volume uncertainty. Table 1 provides an overview of the three source volume estimation methods used in this study and their associated results.

The final seismic magnitudes are M_l 2.6 (AEC); and M_S(VMAX) 3.3 and M_l 2.9 (NEIC) (https://earthquake.usgs.gov/earthquakes/eventpage/ak023bt2cfip). Local magnitudes (M_l) underestimate the landslide size as they fail to capture the larger long-period energy. Thus, the final NEIC magnitude of the landslide was estimated using the M_S(VMAX) magnitude scale (Bonner et al., 2006), which focuses on the longer period surface wave signal. Although this is a more appropriate measure due to the dominant surface wave energy in landslide seismograms, this and other magnitude estimates are designed for double-couple (i.e., earthquake) source mechanisms rather than single-force landslide source mechanisms and thus do not carry the same meaning when applied to landslides.

4.2. Sequence of Sub-Events

The relative timing between high-frequency pulses observed in the seismoacoustic data indicates that two smaller events occurred 8 and 3 min prior to the main failure. These two "foreslide" events have similar seismic and infrasound amplitudes and envelopes (Figures 5 and 6) and similar spectral content (Figure S2 in Supporting Information S1), implying that they had similar failure dynamics. Infrasound back azimuths from array processing (refer to Section 3.2) indicate that the source locations of these smaller events are similar to that of the main event. In Figure 6c, additional apparent arrivals are due to multi-pathing in the atmosphere (de Groot-Hedlin et al., 2009)—they do not correspond to additional events. The foreslide events exhibit a small amount of seismic energy in the 15–200 s band (Figure 6a) but much less than the main event, implying that the majority of the mass failed in the main event. However, the infrasound energy of the "mainslide" is only slightly larger than that of the foreslides (Figures S2c and S2d in Supporting Information S1). The difference in seismoacoustic energy partitioning between the foreslides and the mainslide could be due to a difference in failure type or material—for example, foreslides being snow avalanches with relatively greater infrasound production. There is no obvious indication of multiple failures in the post-event satellite imagery; the seismoacoustic data are the only confirmation of multiple events. We note that the automatic long-period location, force inversion, and other subsequent analyses are all performed for the main failure only. This is due to the low signal-to-noise ratio of the signals from the other events, and their lack of auxiliary data (e.g., pre-event deposits overprinted by main failure). However, NEIC systems triggered on foreslide waveforms in addition to main failure waveforms (Figure 5).

In addition to the two small foreslide events, we observed at least one "afterslide" occurring 8 days after the mainslide. The event was fortuitously captured *in progress* in a Planet Labs satellite image on 22 September 2023—a directional billowing dust cloud near the toe is evident—and a corresponding landslide-like seismic signal was observed at 12:39 on station AK.KTH, the closest seismometer to Peters Dome (about 50 km distance) (Figure S3 in Supporting Information S1) as well as stations out to >200 km. The seismic signal amplitude at station AK.KTH is several times smaller than the corresponding amplitudes of the two foreslide events. Despite snowfall which occurred almost immediately after the main failure, the source area and the base of the cirque directly below Peters Dome remained dark and dusty in daily Planet Labs imagery acquired during the interval

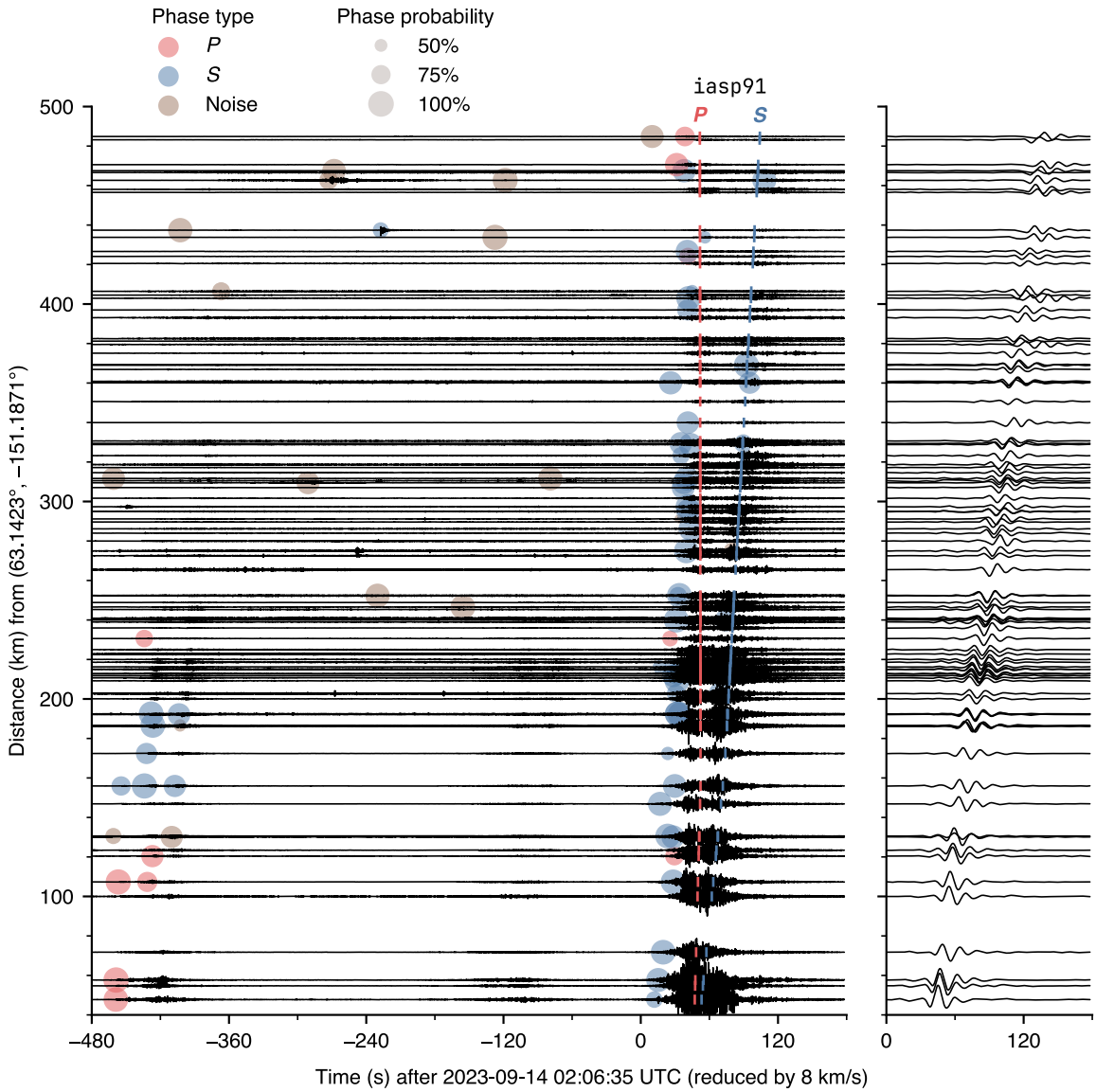

Figure 5. Seismic signature of the Peters Dome landslide. Seismic record sections are shown for high-frequency (1–15 Hz, left panel) and long-period (15–80 s, right panel) waveforms. The time axes are in seconds relative to the estimated main failure origin time of 14 September 2023 02:06:35 UTC. The high-frequency waveform record section is extended earlier in time to show the moveout of the two "foreslide" events at approximately −420 and −120 s. Colored vertical bars indicate arrival times for *P* and *S* phases in the *iasp91* Earth model (Kennett & Engdahl, 1991) relative to the origin time of the main failure plus 45 s. Translucent circles indicate the time of U.S. Geological Survey National Earthquake Information Center (NEIC) waveform triggers. The color and size of the circles correspond to the NEIC phase classifier's predicted phase type (*P*, *S*, or noise) and phase type confidence, respectively.

between the main failure and the afterslide. This indicates that the source region was in fact producing many smaller afterslides in the days following the main failure.

4.3. Main Event Dynamics

Our seismic force inversion and numerical simulation (the latter constrained by both the seismic inversion and the landslide footprint) provide strong constraints on the failure dynamics of the main event (Figure 7). The force inversion fits are robust (Figure S4 in Supporting Information S1), and the jackknife analysis (translucent colored regions in Figure 7) indicates that the result is not very sensitive to changing input data. Recalling that under the assumptions of the single-force mechanism, the force is opposite in direction to the bulk acceleration of the landslide, we observe that the landslide failed initially due north (upward and southward forces), impacting the base of the cirque below Peters Dome at about 20 s (times are relative to the simulation start time). At this point,

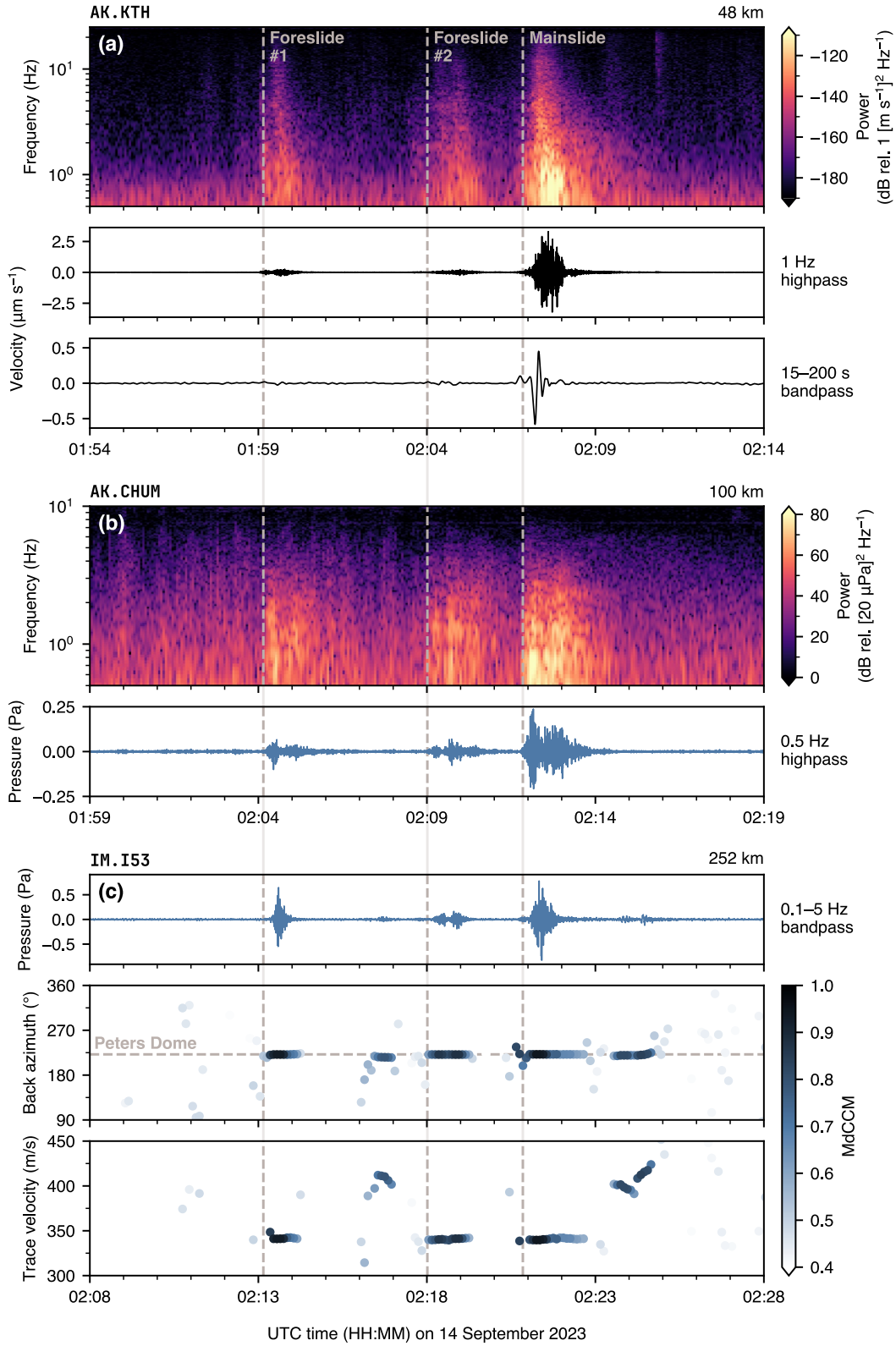

Figure 6.

the mobile material ran up over, and was deflected westward off, the first of two steep ridges protruding into the landslide path, resulting in a downward and eastward force on the Earth. This happened again at 30 s as the flow reached the second ridge, albeit with a smaller vertical force signature. Then, the material decelerated as the flow path curved slightly back eastward, with the final horizontal orientation of the acceleration vector being approximately N–S, subparallel to the initial failure orientation. Fine-scale features observed in $\mathbf{f}(t)$ are not reflected in the trajectory due to the smoothing effect of double integration. The target runout distance for the seismic force inversion trajectory is set at 2.2 km, which is the horizontal distance traversed by the center of mass computed from the numerical simulation.

Our best fitting numerical simulation is achieved for a friction angle $\delta = 16.8°$ and matches the seismic force inversion reasonably well, as shown in Figure 7. Key features, such as dual downward forces and a single sinusoidal cycle of the northward force, are replicated in each time series. The agreement between the numerical model and the force inversion validates our interpretation of event dynamics. Note the mismatch for the first 15 s of upward and northward force time series: the seismic inversion has a very gradual onset, whereas the simulated force is quite sudden. This mismatch is likely due to the instantaneous "dam break" failure implemented by SHALTOP, which causes an impulsive force which becomes smoothed by filtering in post-processing. It is also related to the overestimation of flow acceleration in depth-averaged shallow models due to the neglected slope-perpendicular acceleration (i.e., hydrostatic approximation) (Mangeney-Castelnau et al., 2005). The time snapshot panels in Figure 7 show images of vertical landslide thickness. At 20 s, the bulk of the deposit just begins to impact the first of the two steep ridges. At 40 s, the material has just passed the second ridge. This is consistent with our interpretation of the force time series. The lower portion of the deposit exhibits longitudinal ridges. These are related to longitudinal furrows on the glacier, rather than an intrinsic feature of the failure. An animation of Figure 7 is provided in Movie S1.

By comparing the time of impact between the two ridges—as conveyed by the dual downward/eastward force signals at about 20 and 30 s in Figure 7—and measuring the distance between them, we estimate a center-of-mass speed of 60–70 m/s during this portion of the flow. The larger vertical force for the first ridge impact signal is explained by the higher energy associated with the initial failure from the high source area. This speed is consistent with peak center-of-mass speeds of 64 m/s and 69 m/s obtained from the numerical model and force inversion, respectively. The peak speed of the front of the flow, derived from the numerical model, is 62 m/s.

4.4. Mobility Insights From Numerical Modeling

The good match between the numerically simulated force and the force inverted from seismic data provides several insights into the Peters Dome landslide. The landslide appears to be mainly due to one released mass event because several sub-events would have had a signature on the seismically inverted force. Another key point relates to the friction coefficient μ needed to reproduce the observed deposit and dynamics (i.e., the seismically inverted force). This coefficient reflects the properties of the material involved. Lucas et al. (2014) proposed a simple law to assess the empirical friction coefficient to be used in shallow depth-averaged numerical models with Coulomb friction, in order to reproduce the runout distance of many sub-aerial granular-type landslides. This law, $\mu = V^{-0.0774}$, relates the landslide volume V to the friction coefficient μ. The friction coefficient can be converted to an effective friction angle using Equation 2. For a volume of 6.1 million m^3—the numerical simulation source volume—this empirical relationship predicts a friction angle $\delta = 16.6°$. This agrees well with the optimal numerical simulation's friction angle of 16.8°.

The best-fitting density used for our numerical simulation is 1,100 kg/m^3. Assuming a rock (granite; Wilson et al., 2015) density of 2,700 kg/m^3, the volume fraction of rock in the avalanche can be estimated for various non-

Figure 6. Selected seismic and infrasound signals highlighting the two "foreslides" and the main failure of the Peters Dome landslide. (a) Seismic spectrogram, high-frequency signal, and long-period signal from station AK.KTH, 48 km from the landslide—the closest seismometer. (b) Infrasound spectrogram and high-frequency signal from station AK.CHUM, 100 km from the landslide—the closest infrasound sensor with a visible signal. (c) Infrasound array processing results from array IM.I53, 252 km from the landslide. The back azimuth is the direction, measured clockwise from north, from which infrasound waves arrive (horizontal gray dashed line highlights the back azimuth to Peters Dome). The trace velocity is the apparent speed of incident waves across the array; higher values indicate a steeper arrival angle relative to horizontal. MdCCM stands for median cross-correlation maxima and represents the coherence of waves incident on the array. For (a–c), common time axes for each station are shifted for wave propagation to align to the event sequence. Vertical gray dashed lines, also shifted for wave propagation, highlight the timing of the three landslide events.

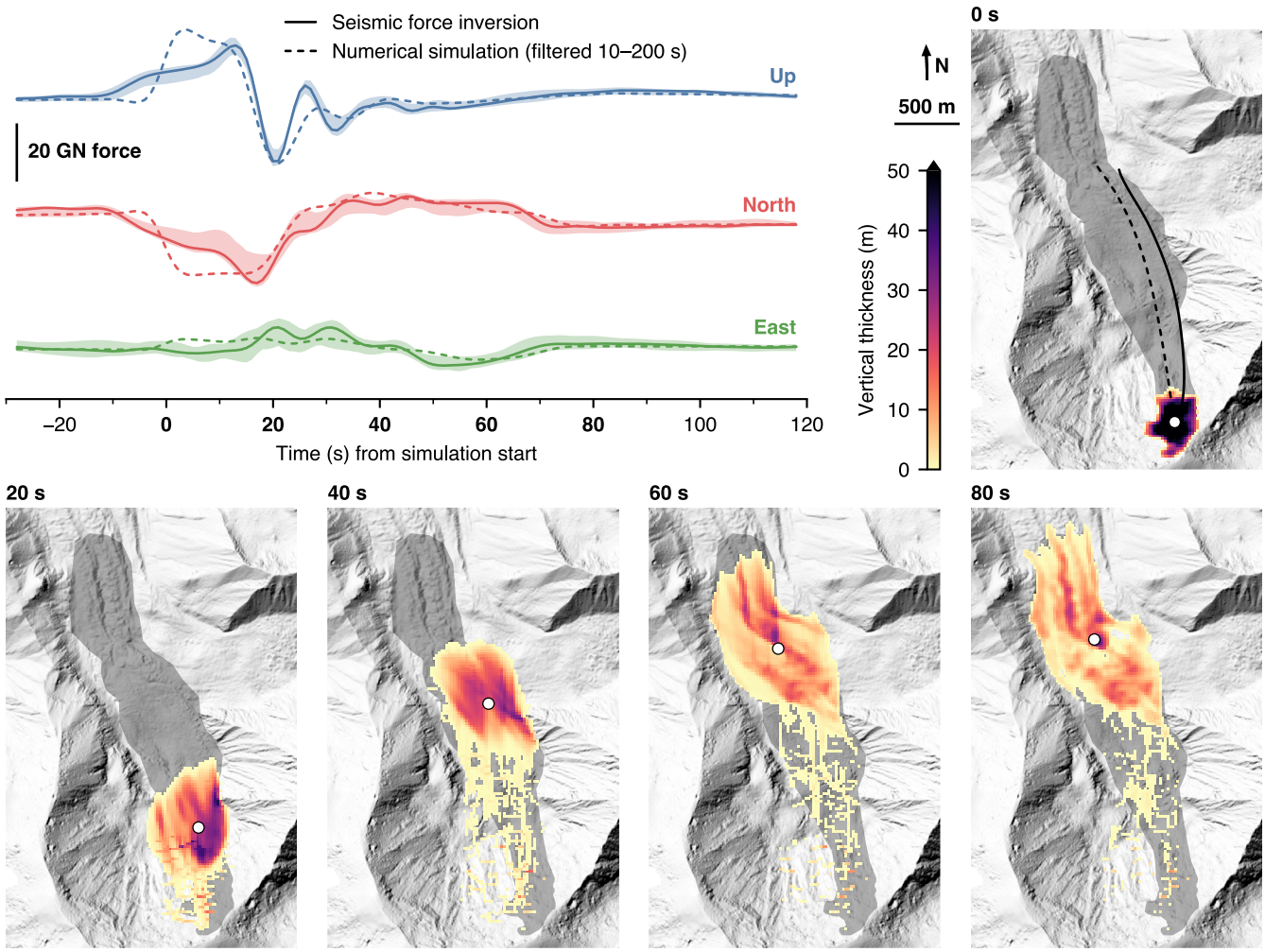

Figure 7. Comparison of the Peters Dome landslide seismic inversion and numerical simulation force time series **f**(t), and numerical simulation thickness time snapshots. **f**(t) represents the forces exerted on the Earth by the landslide. The translucent colored regions surrounding the inversion force time series are the bounds of all jackknife runs (refer to Section 3.4). The solid and dashed black lines in the simulation $t = 0$ s snapshot are the horizontal center-of-mass trajectories from the seismic inversion and the numerical simulation, respectively. White circles mark the numerical simulation center-of-mass location at each plotted time step. The gray translucent patch in all time snapshots is the measured total landslide area. The shaded relief topography is the ArcticDEM from 3 November 2020 (refer to Section 3.6). An animated version of this figure is provided in Movie S1.

rock constituent components. If the non-rock component of the avalanche is ice (920 kg/m^3), this implies a 10% rock volume fraction. If the non-rock component is instead firn (500 kg/m^3; Braithwaite et al., 1994), the rock volume fraction increases to approximately 30%. Horizontal layering visible in freshly exposed vertical snow faces near the headscarp area (Figure 2d) may support the presence of firn. However, given uncertainties in the true composition of materials in the source area, the above analysis represents only a rough guiding estimate of composition. Furthermore, mobile material composition changes during the failure, such as entrainment, deposition, or phase change processes, alter the seismic signature (and thus, the inverted force signature and inferred density) (Favreau et al., 2010; Moretti et al., 2012). Still, this broadly underscores the ability of the joint seismic force inversion and numerical simulation approach to constrain landslide composition.

The friction coefficient of an ice–rock mixture has been shown to decrease with ice content (Zhou et al., 2024). Given the relatively large inferred ice (or compacted snow) concentration, it might be expected that this event would be more mobile than its H/L ratio of 0.38 indicates. However, the rough texture of the glacier onto which the deposit traveled (e.g., refer to Figures 2b and 2c) could be responsible for reducing mobility. Brideau et al. (2021) derived an empirical relationship between H/L ratio and volume for rock avalanches onto unglaciated (280 events) and glaciated (53 events) terrain. The Peters Dome landslide falls within the central mobility range

Table 2
Summary of Methods Applied in This Study Indicating the Data and Conditions Required for Application to New Landslide Events

Method	Data required	Applicable to	Conditions required	Delay to result
Earthquake system detection (Section 3.1)	Seismic waveforms	Large, extremely rapid landslides	Impulsive impact-style failure	Near real-time (min)
Infrasound array processing (Section 3.2)	Infrasound waveforms	Extremely rapid landslides	Favorable infrasound propagation, landslide–array distance proportional to landslide size	Near real-time (min)
Long-period seismic detection (Section 3.3)	Seismic waveforms	Large, extremely rapid landslides	–	Near real-time (min)
Long-period seismic force inversion (Section 3.4)	Seismic waveforms, approximate landslide location	Large, extremely rapid landslides	Sufficient seismic station coverage	Hours to days
SAR amplitude analysis (Section 3.5)	One or more SAR amplitude images	All landslides	Favorable timing and look direction of satellite pass(es)	Days
DEM differencing (Section 3.6)	Pre- and post-event DEMs	All landslides	–	Days to weeks
Numerical flow modeling (Section 3.7)	DEM, 3-D source geometry	Extremely rapid landslides	–	Days to weeks

Note. In this context, "large" indicates a volume >0.1 million m^3, and "extremely rapid" indicates speeds >5 m/s (Hungr et al., 2014).

for unglaciated runout events, but is relatively less mobile for avalanches onto glaciated terrain (refer to Figure 5 in Brideau et al. (2021)), supporting the idea that the rough glacier texture affected mobility.

4.5. Benefits of Joint Seismoacoustic Interpretation

Joint seismic and infrasound analysis of the Peters Dome landslide provides greater constraint on its failure sequence and dynamics than the application of seismic or infrasound data independently. We emphasize this point through several examples. First, the location of this event was determined initially via several different seismic methods (long-period backprojection; traditional seismic phase picks) and from infrasound array analysis. None of these methods were precise enough to identify the specific failure slope. However, the seismic force inversion provided an indication of the failure direction, which in turn constrained the aspect of the slope hosting the failure to be north-facing. This result, combined with basic geomorphological constraints, narrowed down the set of possible failure locations. Second, the failure sequence of this event was determined using both seismic and infrasound methods. The presence of several transients in the near-source seismic data hinted at multiple events, but at the time these were only observed on a single station and their source process (e.g., surficial event) was not clear. The multiple event sequence was confirmed only once we had associated these foreslide events with the same source location, which was accomplished using distal infrasound array analysis (Figure 6c). Then, the seismic data allowed us to conclude that the two foreslides were similar to each other in size and much smaller than the main landslide. Overall, the remarkable quality and quantity of both seismic *and* infrasound data for the Peters Dome landslide enabled us to explore the joint analysis of these two complementary data streams for a large and remote landslide—a rare opportunity.

5. Applicability to Other Events and Geophysical Networks

The degree of remote constraint on this event was high. This motivates inspection of this event and its characterization process to understand how the event's intrinsic properties and the availability of remote data (e.g., seismic, infrasound, imagery) contributed to this relatively thorough event characterization. We are also motivated to consider how transferable the rapid capabilities we used are to other events and if there are particularities of this event that made it more amenable to rapid detection and characterization than other large, extremely rapid events. Table 2 provides an overview of the methods used in this study and highlights their general requirements for application.

5.1. Event Prerequisites for Various Methods

The Peters Dome landslide was a large and extremely rapid event. These traits are a requirement for the subset of the analyses we present which use long-period seismic waves, as remotely observable energy at those frequencies is only generated by large and extremely rapid landslides. Hence, long-period backprojection and seismic force inversions are limited to such events. Other techniques, such as infrasound array processing and imagery analysis, are feasible for much smaller events, especially at shorter source–station distances, but produce best results for larger extremely rapid events because, broadly speaking, seismoacoustic wave energy and deposit size increase with event size. This produces higher signal-to-noise ratios (SNR) for waveform data and more obvious deposits visible in spatially coarser imagery. Future work is required to understand the lower limits on landslide size and speed for seismic and infrasound characterization to be feasible given typical regional (10–100s of km) network configurations. This would help establish a "magnitude of completeness" for seismic detection of landslides, analogous to that for earthquakes (Rydelek & Sacks, 1989).

A distinct feature of the seismic waveforms from this event was the presence of relatively robust body wave (*P* and *S*) arrivals (Figure 5). Such clear first arrivals are uncommon for most landslide processes, as these types of events typically produce emergent arrivals where distinct body wave picks are imperceptible, but clear body wave arrivals have been observed for some events, especially impulsive types of landslides such as rockfalls (Allstadt et al., 2018; Fuchs et al., 2018). The presence of clear body wave arrivals allowed automated near-real-time systems such as that operated by the NEIC to detect this event and derive a first location within 6 km of the true location (Figure 1). The detection was made possible by numerous "triggers" occurring on waveforms from many stations surrounding the event (circles in Figure 5). NEIC detection algorithms are designed to trigger on impulsive earthquake phase arrivals; evidently, the landslide phase arrivals in this case were sufficiently impulsive. A possible explanation for this event's production of relatively clear body waves is the steep drop occurring at the beginning of the failure. This produced an impact force dipping at approximately 60° (at about 20 s; refer to Figure 7), which may contribute to the more impulsive nature of the body wave transients, though we note that the true force angle is best reflected in the topographic slope of the source region, which is about 45°. Interestingly, the deep-learning-based NEIC pick classifier (Section 3.1) labeled most of the true *P* phase arrivals from this event as *S* phase arrivals with relatively high confidence (Figure 5). This may be due to the relatively less impulsive nature of the landslide *P* arrivals relative to the earthquake *P* arrivals used to train the pick classifier—for example, the classifier does not generalize well to non-earthquake sources. This poor generalization limits the ability of such classifiers to enable usable downstream products (e.g., event association and location) for seismogenic landslides. Collectively, the observations for the Peters Dome landslide motivate the development of focused machine learning waveform classification tools specifically trained on verified *landslide* seismic signals.

The rarity of clear first arrivals for many other landslides indicates that the 24/7 earthquake monitoring methods that gave us such an early detection for this event may not work as well for many other large, extremely rapid landslide events without additional tuning and testing. Custom landslide methods, like that introduced in Ekström and Stark (2013) and the AEC long-period backprojection tool (Karasözen & West, 2024), sidestep some of these issues, but they typically have delays of a few minutes (required to, e.g., process sufficient lengths of data and send emails) and are not yet fully integrated into operational monitoring. Still, successful examples of timely detections (e.g., for tsunamigenic landslides in Alaska; Karasözen et al., 2025) highlight the potential of automated seismic and infrasound monitoring—specifically, the use of fast-traveling geophysical waves recorded and telemetered in near real-time to enable expeditious warning.

5.2. Geophysical Network Controls

In addition to event size and speed, geophysical network configurations control detection thresholds and characterization capability. Smaller events require denser networks because their higher-frequency radiation, which attenuates more rapidly, and their lower amplitudes at the source, both result in lower SNR. Alaska is fortunate to host a robust multi-parametric geophysical network composed primarily of earthquake (AEC; network code AK), volcano (AVO; network code AV), and legacy EarthScope Transportable Array (Busby & Aderhold, 2020; adopted as network codes AK and AV, formerly TA) stations, resulting in relatively dense seismic and infrasound coverage. In other areas, such as Greenland, where networks are sparser, only the largest events may be detected (e.g., Svennevig et al., 2024).

5.3. Infrasound Propagation Considerations

An additional consideration for infrasound monitoring specifically is that atmospheric propagation conditions can vary rapidly in space and time (Drob et al., 2003; Iezzi et al., 2019). Thus, detection capability is temporally variable. Denser infrasound networks reduce source–station propagation distances, which can reduce the effect of atmospheric propagation (Toney et al., 2023). However, topography also affects infrasound propagation, particularly at local scales (Lacanna & Ripepe, 2013). For this event, there were three individual infrasound sensors within 100 km of the source—AK.L22K, AK.CUT, and AK.CHUM. Only AK.CHUM (∼100 km distance) recorded a clearly visible signal. Whether this is related to atmospheric or topographic propagation is not clear: AK.L22K and AK.CUT are on the south side of the Alaska range and do not have the signal enhancement capabilities of the infrasound arrays farther south. Combining seismic and infrasound detection capabilities remains a challenge due to uncertainty in time-varying infrasound propagation.

However, we assert that infrasound remains a key aspect of a complete monitoring approach because landslides are a surficial process that interacts with the atmosphere—infrasound processing complements seismic methods. Existing monitoring technologies and networks used for applications like volcano hazards, where infrasound is an established monitoring tool, may be adopted for use in landslide monitoring contexts. For example, arrays AV.KENI and IM.I53 detected this event but were expressly installed for volcano and nuclear test monitoring, respectively. Conversely, arrays AV.WHTR and AV.BAEI were primarily installed for landslide monitoring. AV.BAEI was installed for local monitoring of processes related to the slow-moving Barry Arm landslide (Schaefer et al., 2023), yet it proved useful for regional detection of the Peters Dome landslide.

5.4. Remote Sensing Imagery: Benefits and Limitations

Our response to this event benefited from direct observation via aerial reconnaissance within 24 hr, which provided us with a verified location and source and deposit details. This is rare for large, remote Alaska landslides. Optical imagery has revisit rates (time between successive images of the same location) as rapid as ∼24 hr, but usable imagery is weather-dependent, which is a challenge for the mountainous terrain where landslides often occur. Our response leveraged SAR imagery, which is not affected by cloud cover (Mondini et al., 2021). However, the current Sentinel-1 revisit rate is ∼12 days (our post-event image was acquired 7 days after the event). Stereo optical imagery pairs used for DEM creation have irregular revisit rates, are not publicly available, and can be difficult to process in steep, shadowed terrain and/or glacial environments. Increased revisit rates will improve the remote sensing timeline in the future, but with current technologies, we believe that rapid response (i.e., timescale of minutes) is the domain of seismology and infrasound.

However, given seismoacoustic location method uncertainties, there are additional improvements required to zero in on the exact affected slope without additional confirmation from remote sensing or field reconnaissance. Long-period seismic force inversions can provide some constraint on failure direction, but automating these approaches is a challenge due to the careful station selection, data processing, and parameter choices currently required to obtain a robust result (Toney & Allstadt, 2021). Despite their temporal disadvantage, we emphasize that imagery-based remote sensing products and on-site visits are still essential for cultivating a deeper and more complete understanding of failure mechanism and material properties, as well as for validating remotely assessed landslide parameters. Furthermore, these more detailed products are often the only way to understand actual impacts (e.g., building hit, road covered, etc.).

5.5. Role of Numerical Simulations

Finally, landslide simulations, when constrained with seismic and geological data such as those presented here, make it possible to verify hypotheses on landslide dynamics such as the number of sub-events, peak velocities, the influence of ice on dynamics, and the nature of the flow (e.g., frictional vs. viscous). Currently, available landslide models such as SHALTOP can be used to rapidly simulate landslide events provided that a DEM and source geometry are available. For sufficiently large events, force inversions generated using long-period seismic waves provide a powerful constraint on numerical model parameters. In turn, such robust numerical simulations can provide vivid reconstructions of failure dynamics for even the most remote events, including key information such as flow front speed and height and basal friction. These insights into dynamics and mechanical behavior cannot be obtained from traditional imagery-based remote sensing techniques, yet they are invaluable for informing hazard assessment of future similar events.

6. Implications for Future Landslide Responses: Communication and Collaboration

Large landslides have always been part of the hazard landscape of Alaska. But new federal investment and coordination since 2020 (e.g., the National Landslide Preparedness Act; Godt et al., 2022), has fundamentally changed both monitoring and response. Prior to this, large landslides in the state were followed by healthy, but ad hoc, coordination between well-intentioned colleagues. There was neither a mechanism, nor financial support, for systematic analysis and follow-up. However, Alaska is evolving rapidly in the direction of a well-structured landslide monitoring program. The Peters Dome landslide well illustrates several of the elements that are important for the success of such a program. In this section, we highlight those elements and make generalized recommendations for future responses.

A critical element in this response was the presence of established communication channels. Scientists in the natural hazards space typically maintain a portfolio of contacts and preferred communication channels (text, social media, email, phone, etc.). But in the Peters Dome landslide case, several of this article's authors, and dozens of other scientists, were already connected via messaging platforms commonly used within the AEC and AVO. In addition to already being subscribed, those who used these platforms had several years of experience and knew where to put rapidly evolving information and discussion to be certain it reached key people quickly. However, no emergency response communication is perfect, and neither was this one. Collaborators outside the AEC and AVO either used a different messaging platform or just email and phone calls, with email being the most universal connector between agencies. The use of email, however, had some drawbacks: Overlapping threads and differing recipient lists made it difficult for any one person to receive all the information. This resulted in some parallel efforts and typically slower response times. Hence, the Peters Dome landslide response benefitted from the use of non-email communication platforms. For future responses, a common, mobile- and desktop-friendly, easy-to-use, and configurable messaging platform could be beneficial to encourage timely and inclusive communication across organizations.

A second successful element was the existence of people (i.e., positions) with job expectations for landslide response. In the Peters Dome landslide case, several people had both the bandwidth and the responsibility to focus entirely on the landslide and its implications. The 24-hr timeline of products outlined in Section 2 and Text S1 in Supporting Information S1, and shown in Figure 3, demonstrates this. The other benefit of having staff positions dedicated to response is the intuition and situational awareness that is built over time. Some of the same staff responding to the Peters Dome landslide had worked together through several large landslides in the past few years. Because of this, the group had context for the size, rarity, and likely impacts of this landslide even before all the details were known. This observation indicates that the establishment of formal protocols for geophysical landslide monitoring could be especially beneficial within agencies already routinely monitoring other hazards, such as earthquakes.

The last element of success demonstrated by this landslide response is the value of partnerships between agency and academic partners. Each brings unique resources. For example, it was the rigor of NEIC's 24/7 earthquake review processes, coupled with the formalism of the USGS's ANSS, that triggered coordination with the AEC's duty seismologist within tens of minutes after the Peters Dome landslide. The comparative nimbleness and local knowledge of university partners quickly engaged DNPP staff, which led to the notably rapid collection of photos from the site. Future responses can benefit from transparent communication between agency and academic groups to ensure the timeliest and most scientifically robust actions and interpretations are performed.

7. Conclusions

The 13 September 2023 Peters Dome ice–rock avalanche produced robust seismic and infrasound signals, which were recorded at distances exceeding 250 km. These signals contributed to the rapid detection of the event through both standard earthquake monitoring systems and a specialized landslide detection algorithm. The automated detection by the earthquake operational systems was of particular note because this has not historically been common for landslides. This event highlights how remotely acquired seismic and infrasound data are complementary and can be used to determine the source properties of large landslides, potentially in the absence of direct observations. Prior to any aerial or satellite imagery (the typical way to verify these events), the approximate location, time of failure, direction of failure, and basic dynamics of this event were determined from seismoacoustic records alone. As seismoacoustic network coverage increases globally, and algorithms improve, these sensing modalities can become increasingly useful for landslides. Large, well-recorded events such as the

Peters Dome landslide serve as important benchmarking events for testing cross-disciplinary approaches and automated monitoring systems in the rapidly advancing field of seismoacoustic landslide monitoring. In addition, landslide simulations with current numerical models can constrain landslide properties more finely. Conversely, well-constrained events such as the Peters Dome landslide can be used to benchmark and validate such models. The interagency coordination required by the response to this event offers additional lessons that highlight the value of well-established communication channels, staff with prior response experience and professional protocols to respond quickly, and the complementary assets of agency and academic partners.

Conflict of Interest

The authors declare no conflicts of interest relevant to this study.

Availability Statement

All seismic and infrasound data used in this study are distributed openly. They are available through the facilities of the EarthScope Consortium under International Federation of Digital Seismograph Networks network codes AK (Alaska Earthquake Center, University of Alaska Fairbanks, 1987), AT (National Oceanic and Atmospheric Administration, 1967), AV (Alaska Volcano Observatory/USGS, 1988), IM (Various institutions, 1965), and IU (Albuquerque Seismological Laboratory/USGS, 1988). Sentinel-1 images were processed with ASF DAAC HyP3 2024 using the hyp3_gamma plugin version 8.0.1 running GAMMA release 20230712. This work uses modified Copernicus Sentinel data 2023, processed by ESA. We used the *lts_array* code (https://github.com/uafgeotools/lts_array; Bishop et al., 2020) to perform infrasound array processing. We used some utility functions of *digger* (Barnhart et al., 2024) in this work. The SHALTOP code has restricted access. SHALTOP simulation output used in this work is included in the data release associated with this publication, which is available at Toney et al. (2026).

Acknowledgments

This article was greatly improved by constructive comments from Erin Jensen, Johannes Leinauer, William Yeck, Eric Bilderback, Kristen Marra, and two anonymous reviewers. We thank seismic analysts at the NEIC and AEC for their work on the seismic data from this event, and William Yeck for providing us with NEIC automated phase picks. Denali Air pilot Aine Roberts captured the earliest photographic evidence of this event. We are grateful to pilot Justin Wiseman and National Park Service Geographic Information System Specialist Britta Schroeder for rapidly mobilizing an aerial reconnaissance flight. We thank Paula Bürgi and Lauren Schaefer for their assistance with interpreting the SAR amplitude imagery. Support for E. K. and M. W. was provided by USGS agreement #G00014775 and the Office of the Alaska State Seismologist. A. M. was supported by the Marie Skłodowska-Curie Actions Doctoral Network EnvSeis consortium (grant agreement 101073148). Seismic data recorded by the Alaska Earthquake Center is made possible by USGS ANSS program cooperative agreement G22AC00001 and National Science Foundation (NSF) award 2024208. Some DEMs used in this work were provided by the Polar Geospatial Center under NSF-OPP awards 1043681, 1559691, 1542736, 1810976, and 2129685. Any use of trade, firm, or product names is for descriptive purposes only and does not imply endorsement by the U.S. Government.

References

Alaska Earthquake Center, University of Alaska Fairbanks. (1987). Alaska Geophysical Network [Dataset]. *International Federation of Digital Seismograph Networks*. https://doi.org/10.7914/SN/AK

Alaska Volcano Observatory/USGS. (1988). Alaska Volcano Observatory [Dataset]. *International Federation of Digital Seismograph Networks*. https://doi.org/10.7914/SN/AV

Albuquerque Seismological Laboratory/USGS. (1988). Global Seismograph Network [Dataset]. *International Federation of Digital Seismograph Networks*. https://doi.org/10.7914/SN/IU

Allstadt, K. E. (2013). Extracting source characteristics and dynamics of the August 2010 Mount Meager landslide from broadband seismograms. *Journal of Geophysical Research: Earth Surface*, *118*(3), 1472–1490. https://doi.org/10.1002/jgrf.20110

Allstadt, K. E., & Toney, L. (2020). Isforce [Computer software]. *U.S. Geological Survey*. https://doi.org/10.5066/P9CR20KW

Allstadt, K. E., Coe, J. A., Collins, E., Rengers, F. K., Mangeney, A., Esser, S. M., et al. (2024). The 2022 Chaos Canyon landslide in Colorado: Insights revealed by seismic analysis, field investigations, and remote sensing. *Landslides*, *21*(2), 309–325. https://doi.org/10.1007/s10346-023-02179-4

Allstadt, K. E., Matoza, R. S., Lockhart, A. B., Moran, S. C., Caplan-Auerbach, J., Haney, M. M., et al. (2018). Seismic and acoustic signatures of surficial mass movements at volcanoes. *Journal of Volcanology and Geothermal Research*, *364*, 76–106. https://doi.org/10.1016/j.jvolgeores.2018.09.007

Barnhart, K. R., George, D. L., Collins, A. L., & Amaral, T. (2024). digger—Utility tools for landslide runout modeling (Version 1.1) [Computer software]. *U.S. Geological Survey*. https://doi.org/10.5066/P14TUMBB

Bessette-Kirton, E. K., & Coe, J. A. (2020). A 36-year record of rock avalanches in the Saint Elias Mountains of Alaska, with implications for future hazards. *Frontiers in Earth Science*, *8*, 293. https://doi.org/10.3389/feart.2020.00293

Bishop, J. W., Fee, D., & Szuberla, C. A. L. (2020). Improved infrasound array processing with robust estimators. *Geophysical Journal International*, *221*(3), 2058–2074. https://doi.org/10.1093/gji/ggaa110

Bonner, J., Russell, D., Harkrider, D., Reiter, D., & Herrman, R. (2006). Development of a time-domain, variable-period surface-wave magnitude measurement procedure for application at regional and teleseismic distances, part II: Application and M_s-m_b performance. *Bulletin of the Seismological Society of America*, *96*(2), 678–696. https://doi.org/10.1785/0120050056

Braithwaite, R. J., Laternser, M., & Pfeffer, W. T. (1994). Variations of near-surface firn density in the lower accumulation area of the Greenland ice sheet, Pâkitsoq, West Greenland. *Journal of Glaciology*, *40*(136), 477–485. https://doi.org/10.3189/S002214300001234X

Brideau, M.-A., De Vilder, S., Massey, C., Mitchell, A., McDougall, S., & Aaron, J. (2021). Empirical relationships to estimate the probability of runout exceedance for various landslide types. In F. Guzzetti, S. Mihalić Arbanas, P. Reichenbach, K. Sassa, P. T. Bobrowsky, & K. Takara (Eds.), *Understanding and reducing landslide disaster risk* (pp. 321–327). Springer International Publishing. https://doi.org/10.1007/978-3-030-60227-7_36

Busby, R. W., & Aderhold, K. (2020). The Alaska transportable array: As built. *Seismological Research Letters*, *91*(6), 3017–3027. https://doi.org/10.1785/0220200154

Chang, J.-M., Kuo, Y.-T., Chao, W.-A., Lin, C.-M., Lan, H.-W., Yang, C.-M., & Chen, H. (2024). Landslide warning area delineation through seismic signals and landslide characteristics: Insights from the Silabaku landslide in southern Taiwan. *Seismological Research Letters*, *95*(5), 2986–2996. https://doi.org/10.1785/0220230396

Chao, W.-A., Wu, Y.-M., Zhao, L., Chen, H., Chen, Y.-G., Chang, J.-M., & Lin, C.-M. (2017). A first near real-time seismology-based landquake monitoring system. *Scientific Reports*, *7*(1), 43510. https://doi.org/10.1038/srep43510

Coe, J. A., Bessette-Kirton, E. K., & Geertsema, M. (2018). Increasing rock-avalanche size and mobility in Glacier Bay National Park and Preserve, Alaska detected from 1984 to 2016 Landsat imagery. *Landslides*, *15*(3), 393–407. https://doi.org/10.1007/s10346-017-0879-7

Corominas, J. (1996). The angle of reach as a mobility index for small and large landslides. *Canadian Geotechnical Journal*, *33*(2), 260–271. https://doi.org/10.1139/t96-005

Costa, J. E., & Schuster, R. L. (1988). The formation and failure of natural dams. *Geological Society of America Bulletin*, *100*(7), 1054–1068. https://doi.org/10.1130/0016-7606(1988)100<1054:TFAFON>2.3.CO;2

de Groot-Hedlin, C. D., Hedlin, M. A. H., & Drob, D. P. (2009). Atmospheric variability and infrasound monitoring. In A. Le Pichon, E. Blanc, & A. Hauchecorne (Eds.), *Infrasound monitoring for atmospheric studies* (1st ed., pp. 475–507). Springer Netherlands.

De Negri, R., & Matoza, R. S. (2023). Rapid location of remote volcanic infrasound using 3D ray tracing and empirical climatologies: Application to the 2011 Cordón Caulle and 2015 Calbuco eruptions, Chile. *Journal of Geophysical Research: Solid Earth*, *128*(3), e2022JB025735. https://doi.org/10.1029/2022JB025735

Drob, D. P., Picone, J. M., & Garcés, M. (2003). Global morphology of infrasound propagation. *Journal of Geophysical Research*, *108*(D21), 1–12. https://doi.org/10.1029/2002JD003307

Dufresne, A., Wolken, G. J., Hibert, C., Bessette-Kirton, E. K., Coe, J. A., Geertsema, M., & Ekström, G. (2019). The 2016 Lamplugh rock avalanche, Alaska: Deposit structures and emplacement dynamics. *Landslides*, *16*(12), 2301–2319. https://doi.org/10.1007/s10346-019-01225-4

Ekström, G., & Stark, C. P. (2013). Simple scaling of catastrophic landslide dynamics. *Science*, *339*(6126), 1416–1419. https://doi.org/10.1126/science.1232887

Favreau, P., Mangeney, A., Lucas, A., Crosta, G., & Bouchut, F. (2010). Numerical modeling of landquakes. *Geophysical Research Letters*, *37*(15), L15305. https://doi.org/10.1029/2010GL043512

Freymueller, J. T., & West, M. E. (2024). EarthScope networks in Alaska and northwestern Canada. In N. A. Ruppert, M. A. Jamadec, & J. T. Freymuller (Eds.), *Tectonics and seismic structure of Alaska and northwestern Canada: EarthScope and beyond*. Wiley. https://doi.org/10.1002/9781394195947.ch1

Fuchs, F., Lenhardt, W., Bokelmann, G., & the AlpArray Working Group. (2018). Seismic detection of rockslides at regional scale: Examples from the Eastern Alps and feasibility of kurtosis-based event location. *Earth Surface Dynamics*, *6*(4), 955–970. https://doi.org/10.5194/esurf-6-955-2018

Galas, S., Dalbey, K., Kumar, D., Patra, A., & Sheridan, M. (2007). Benchmarking TITAN2D mass flow model against a sand flow experiment and the 1903 Frank Slide. In *Proceedings of the 2007 International Forum on Landslide Disaster Management* (pp. 899–918).

Gauthier, D., Anderson, S. A., Fritz, H. M., & Giachetti, T. (2018). Karrat Fjord (Greenland) tsunamigenic landslide of 17 June 2017: Initial 3D observations. *Landslides*, *15*(2), 327–332. https://doi.org/10.1007/s10346-017-0926-4

Geertsema, M. (2012). Initial observations of the 11 June 2012 rock/ice avalanche, Lituya Mountain, Alaska. In *The First Meeting of Cold Region Landslides Network, Harbin, China*. https://doi.org/10.13140/2.1.2473.5682

George, D., Iverson, R. M., & Cannon, C. (2022). *Modeling the dynamics of lahars that originate as landslides on the west side of Mount Rainier, Washington* (USGS Open-File Report 2021–1118). U.S. Geological Survey. https://doi.org/10.3133/ofr20211118

Godt, J., Wood, N. J., Pennaz, A., Dacey, C. M., Mirus, B. B., Schaefer, L. N., & Slaughter, S. L. (2022). *National strategy for landslide loss reduction* (USGS Open-File Report 2022–1075). U.S. Geological Survey. https://doi.org/10.3133/ofr20221075

Hayes, G., Earle, P., Benz, H., Wald, D., & Yeck, W. (2019). *National Earthquake Information Center strategic plan, 2019–23* (USGS Circular 1457). U.S. Geological Survey. https://doi.org/10.3133/cir1457

Hibert, C., Ekström, G., & Stark, C. P. (2017). The relationship between bulk-mass momentum and short-period seismic radiation in catastrophic landslides. *Journal of Geophysical Research: Earth Surface*, *122*(5), 1201–1215. https://doi.org/10.1002/2016JF004027

Hibert, C., Michéa, D., Provost, F., Malet, J.-P., & Geertsema, M. (2019). Exploration of continuous seismic recordings with a machine learning approach to document 20 yr of landslide activity in Alaska. *Geophysical Journal International*, *219*(2), 1138–1147. https://doi.org/10.1093/gji/ggz354

Higman, B., Shugar, D. H., Stark, C. P., Ekström, G., Koppes, M. N., Lynett, P., et al. (2018). The 2015 landslide and tsunami in Taan Fiord, Alaska. *Scientific Reports*, *8*(1), 12993. https://doi.org/10.1038/s41598-018-30475-w

Huggel, C., Caplan-Auerbach, J., Waythomas, C. F., & Wessels, R. L. (2007). Monitoring and modeling ice-rock avalanches from ice-capped volcanoes: A case study of frequent large avalanches on Iliamna Volcano, Alaska. *Journal of Volcanology and Geothermal Research*, *168*(1–4), 114–136. https://doi.org/10.1016/j.jvolgeores.2007.08.009

Huggel, C., Caplan-Auerbach, J., & Wessels, R. (2008). Recent extreme avalanches: Triggered by climate change? *Eos, Transactions American Geophysical Union*, *89*(47), 469–470. https://doi.org/10.1029/2008EO470001

Hungr, O., Leroueil, S., & Picarelli, L. (2014). The Varnes classification of landslide types, an update. *Landslides*, *11*(2), 167–194. https://doi.org/10.1007/s10346-013-0436-y

Iezzi, A. M., Schwaiger, H. F., Fee, D., & Haney, M. M. (2019). Application of an updated atmospheric model to explore volcano infrasound propagation and detection in Alaska. *Journal of Volcanology and Geothermal Research*, *371*, 192–205. https://doi.org/10.1016/j.jvolgeores.2018.03.009

Karasözen, E., & West, M. E. (2024). Toward the rapid seismic assessment of landslides in coastal Alaska. *The Seismic Record*, *4*(1), 43–51. https://doi.org/10.1785/0320230044

Karasözen, E., West, M. E., Barnhart, K. R., Lyons, J. J., Nichols, T., Schaefer, L. N., et al. (2025). 2024 Surprise Inlet landslides: Insights from a prototype landslide-triggered tsunami monitoring system in Prince William Sound, Alaska. *Geophysical Research Letters*, *52*(13), e2025GL115911. https://doi.org/10.1029/2025gl115911

Kennett, B. L. N., & Engdahl, E. R. (1991). Traveltimes for global earthquake location and phase identification. *Geophysical Journal International*, *105*(2), 429–465. https://doi.org/10.1111/j.1365-246X.1991.tb06724.x

Lacanna, G., & Ripepe, M. (2013). Influence of near-source volcano topography on the acoustic wavefield and implication for source modeling. *Journal of Volcanology and Geothermal Research*, *250*, 9–18. https://doi.org/10.1016/j.jvolgeores.2012.10.005

Larsen, I. J., Montgomery, D. R., & Korup, O. (2010). Landslide erosion controlled by hillslope material. *Nature Geoscience*, *3*(4), 247–251. https://doi.org/10.1038/ngeo776

Lee, E.-J., Liao, W.-Y., Lin, G.-W., Chen, P., Mu, D., & Lin, C.-W. (2019). Towards automated real-time detection and location of large-scale landslides through seismic waveform back projection. *Geofluids*, *2019*, 1–14. https://doi.org/10.1155/2019/1426019

Lucas, A., Mangeney, A., & Ampuero, J. P. (2014). Frictional velocity-weakening in landslides on Earth and on other planetary bodies. *Nature Communications*, *5*(1), 3417. https://doi.org/10.1038/ncomms4417

Manconi, A., Mondini, A. C., & the AlpArray working group. (2022). Landslides caught on seismic networks and satellite radars. *Natural Hazards and Earth System Sciences*, *22*(5), 1655–1664. https://doi.org/10.5194/nhess-22-1655-2022

Manconi, A., Picozzi, M., Coviello, V., De Santis, F., & Elia, L. (2016). Real-time detection, location, and characterization of rockslides using broadband regional seismic networks. *Geophysical Research Letters*, *43*(13), 6960–6967. https://doi.org/10.1002/2016GL069572

Mangeney, A., Bouchut, F., Thomas, N., Vilotte, J. P., & Bristeau, M. O. (2007). Numerical modeling of self-channeling granular flows and of their levee-channel deposits. *Journal of Geophysical Research*, *112*(F2), F02017. https://doi.org/10.1029/2006JF000469

Mangeney-Castelnau, A., Bouchut, F., Vilotte, J. P., Lajeunesse, E., Aubertin, A., & Pirulli, M. (2005). On the use of Saint Venant equations to simulate the spreading of a granular mass. *Journal of Geophysical Research*, *110*(B9), B09103. https://doi.org/10.1029/2004JB003161

Marchetti, E., & Johnson, J. B. (2023). Infrasound array analysis of rapid mass movements in mountain regions. In C. Schmelzbach (Ed.), *Advances in geophysics* (Vol. 64, pp. 1–57). Elsevier. https://doi.org/10.1016/bs.agph.2023.06.001

Matoza, R. S., Green, D. N., Le Pichon, A., Shearer, P. M., Fee, D., Mialle, P., & Ceranna, L. (2017). Automated detection and cataloging of global explosive volcanism using the International Monitoring System infrasound network. *Journal of Geophysical Research: Solid Earth*, *122*(4), 2946–2971. https://doi.org/10.1002/2016JB013356

Mitchell, A., Allstadt, K. E., George, D., Aaron, J., McDougall, S., Moore, J., & Menounos, B. (2022). Insights on multistage rock avalanche behavior from runout modeling constrained by seismic inversions. *Journal of Geophysical Research: Solid Earth*, *127*(10), e2021JB023444. https://doi.org/10.1029/2021JB023444

Mondini, A. C., Guzzetti, F., Chang, K.-T., Monserrat, O., Martha, T. R., & Manconi, A. (2021). Landslide failures detection and mapping using Synthetic Aperture Radar: Past, present and future. *Earth-Science Reviews*, *216*, 103574. https://doi.org/10.1016/j.earscirev.2021.103574

Moretti, L., Mangeney, A., Capdeville, Y., Stutzmann, E., Huggel, C., Schneider, D., & Bouchut, F. (2012). Numerical modeling of the Mount Steller landslide flow history and of the generated long period seismic waves. *Geophysical Research Letters*, *39*(16), L16402. https://doi.org/10.1029/2012GL052511

Moretti, L., Mangeney, A., Walter, F., Capdeville, Y., Bodin, T., Stutzmann, E., & Le Friant, A. (2020). Constraining landslide characteristics with Bayesian inversion of field and seismic data. *Geophysical Journal International*, *221*(2), 1341–1348. https://doi.org/10.1093/gji/ggaa056

National Oceanic and Atmospheric Administration. (1967). National Tsunami Warning Center Alaska Seismic Network [Dataset]. *International Federation of Digital Seismograph Networks*. https://doi.org/10.7914/SN/AT

Noh, M.-J., & Howat, I. M. (2017). The Surface Extraction from TIN based Search-space Minimization (SETSM) algorithm. *ISPRS Journal of Photogrammetry and Remote Sensing*, *129*, 55–76. https://doi.org/10.1016/j.isprsjprs.2017.04.019

Peruzzetto, M., Mangeney, A., Bouchut, F., Grandjean, G., Levy, C., Thiery, Y., & Lucas, A. (2021). Topography curvature effects in thin-layer models for gravity-driven flows without bed erosion. *Journal of Geophysical Research: Earth Surface*, *126*(4), e2020JF005657. https://doi.org/10.1029/2020JF005657

Porter, C., Howat, I., Noh, M. J., Husby, E., Khuvis, S., Danish, E., et al. (2023). ArcticDEM – Strips, Version 4.1 [Dataset]. *Harvard Dataverse, V1*. https://doi.org/10.7910/DVN/3VDC4W

Rydelek, P. A., & Sacks, I. S. (1989). Testing the completeness of earthquake catalogues and the hypothesis of self-similarity. *Nature*, *337*(6204), 251–253. https://doi.org/10.1038/337251a0

Schaefer, L. N., Coe, J. A., Wikstrom Jones, K., Collins, B. D., Staley, D., West, M. E., et al. (2023). Kinematic evolution of a large paraglacial landslide in the Barry Arm fjord of Alaska. *Journal of Geophysical Research: Earth Surface*, *128*(11), e2023JF007119. https://doi.org/10.1029/2023JF007119

Svennevig, K., Hicks, S. P., Forbriger, T., Lecocq, T., Widmer-Schnidrig, R., Mangeney, A., et al. (2024). A rockslide-generated tsunami in a Greenland fjord rang Earth for 9 days. *Science*, *385*(6714), 1196–1205. https://doi.org/10.1126/science.adm9247

Toney, L., & Allstadt, K. E. (2021). lsforce: A Python-based single-force seismic inversion framework for massive landslides. *Seismological Research Letters*, *92*(4), 2610–2626. https://doi.org/10.1785/0220210004

Toney, L., Collins, E., & Allstadt, K. E. (2026). Simulation and modeling output and geospatial data from the 2023 Peters Dome landslide (Alaska) [Dataset]. *U.S. Geological Survey*. https://doi.org/10.5066/P13WIS6X

Toney, L., Fee, D., Allstadt, K. E., Haney, M. M., & Matoza, R. S. (2021). Reconstructing the dynamics of the highly similar May 2016 and June 2019 Iliamna Volcano (Alaska) ice–rock avalanches from seismoacoustic data. *Earth Surface Dynamics*, *9*(2), 271–293. https://doi.org/10.5194/esurf-9-271-2021

Toney, L., Fee, D., Schmandt, B., & Bishop, J. W. (2023). Examining infrasound propagation at high spatial resolution using a nodal seismic array. *Journal of Geophysical Research: Solid Earth*, *128*(11), e2023JB027314. https://doi.org/10.1029/2023JB027314

Various institutions. (1965). International miscellaneous stations [Dataset]. *International Federation of Digital Seismograph Networks*. https://doi.org/10.7914/vefq-vh75

Wessel, P., & Smith, W. H. F. (1996). A global, self-consistent, hierarchical, high-resolution shoreline database. *Journal of Geophysical Research*, *101*(B4), 8741–8743. https://doi.org/10.1029/96JB00104

Wilson, F. H., Hults, C. P., Mull, C. G., & Karl, S. M. (2015). *Geologic map of Alaska* (USGS Scientific Investigations Map 3340) [Map]. U.S. Geological Survey. https://doi.org/10.3133/sim3340

Yeck, W. L., Patton, J. M., Ross, Z. E., Hayes, G. P., Guy, M. R., Ambruz, N. B., et al. (2021). Leveraging deep learning in global 24/7 real-time earthquake monitoring at the National Earthquake Information Center. *Seismological Research Letters*, *92*(1), 469–480. https://doi.org/10.1785/0220200178

Zhou, G. G. D., Cui, K. F. E., Jing, L., Mangeney, A., Cui, Y., Huang, Y., & Chen, X. (2024). Segregation-induced flow transitions in rock-ice mixtures: Implications for rock-ice avalanche dynamics. *Journal of Geophysical Research: Earth Surface*, *129*(9), e2024JF007831. https://doi.org/10.1029/2024JF007831